



Sensitivity of simulated CO₂ concentration to sub-annual variations in fossil fuel CO₂ emissions

Xia Zhang^{1,2}, Kevin R. Gurney¹, Peter Rayner³, David Baker⁴, and Yu-ping Liu⁵

¹School of Life Science, Arizona State University, Tempe, AZ, USA

²College of Science, San Diego State University, San Diego, CA, USA

³Earth Sciences, University of Melbourne, Melbourne, Australia

⁴Cooperative Institute for Research in the Atmosphere, Colorado State University, Fort Collins, CO, USA

⁵Laboratory for Atmosphere, Science Systems and Applications, Inc., NASA Goddard Space Flight Center Code 614 Greenbelt, MD, USA

Correspondence to: Xia Zhang (tyouxia@gmail.com)

Received: 8 July 2015 – Published in Atmos. Chem. Phys. Discuss.: 31 July 2015

Revised: 2 February 2016 – Accepted: 8 February 2016 – Published: 19 February 2016

Abstract. Recent advances in fossil fuel CO₂ (FFCO₂) emission inventories enable sensitivity tests of simulated atmospheric CO₂ concentrations to sub-annual variations in FFCO₂ emissions and what this implies for the interpretation of observed CO₂. Six experiments are conducted to investigate the potential impact of three cycles of FFCO₂ emission variability (diurnal, weekly and monthly) using a global tracer transport model. Results show an annual FFCO₂ rectification varying from -1.35 to $+0.13$ ppm from the combination of all three cycles. This rectification is driven by a large negative diurnal FFCO₂ rectification due to the covariation of diurnal FFCO₂ emissions and diurnal vertical mixing, as well as a smaller positive seasonal FFCO₂ rectification driven by the covariation of monthly FFCO₂ emissions and monthly atmospheric transport. The diurnal FFCO₂ emissions are responsible for a diurnal FFCO₂ concentration amplitude of up to 9.12 ppm at the grid cell scale. Similarly, the monthly FFCO₂ emissions are responsible for a simulated seasonal CO₂ amplitude of up to 6.11 ppm at the grid cell scale. The impact of the diurnal FFCO₂ emissions, when only sampled in the local afternoon, is also important, causing an increase of $+1.13$ ppmv at the grid cell scale. The simulated CO₂ concentration impacts from the diurnally and seasonally varying FFCO₂ emissions are centered over large source regions in the Northern Hemisphere, extending to downwind regions. This study demonstrates the influence of sub-annual variations in FFCO₂ emissions on simulated

CO₂ concentration and suggests that inversion studies must take account of these variations in the affected regions.

1 Introduction

Quantification of the spatial and temporal distribution of carbon sources and sinks is critical for projecting future atmospheric CO₂ concentrations and climate change (Field et al., 2007). Inferring exchanges of CO₂ between the atmosphere and the terrestrial biosphere/ocean from atmospheric CO₂ observations, using inverse methods based on atmospheric transport models, has been an important approach (e.g., Tans et al., 1990; Enting, 2002; Gurney et al., 2002).

In atmospheric CO₂ inversions, fossil fuel CO₂ (FFCO₂) emissions are often treated as a known quantity in the system; consequently, uncertainty in FFCO₂ emissions is not considered explicitly and errors in the distribution of simulated atmospheric FFCO₂ are translated into errors in the terrestrial biospheric flux estimates. This problem has not been well studied, due mainly to limitations such as the coarse resolution of traditional FFCO₂ inventories, the sparse monitoring of atmospheric CO₂ concentrations, and sub-grid parameterization of atmospheric transport models. In recent years, significant advances have been made in increasing the density of atmospheric observations and in the accuracy, fidelity and resolution of FFCO₂ inventories. For example, the network of atmospheric high-frequency CO₂ concentration

measurements has grown over the last decade (NACP project in North America and CarboEurope_IP project in Europe). Global FFCO₂ inventories have been produced at high resolution in both the space and time domains – these resolve the CO₂ emissions at spatial scales smaller than 10 km and with hourly time resolution (Rayner et al., 2010; Oda and Maksyutov, 2011; Wang et al., 2013; Nassar et al., 2013; Asefi-Najafabady et al., 2014). These advances provide information that permits a careful examination of how the high-resolution FFCO₂ emission data products impact the spatial and temporal distribution of atmospheric CO₂ and flux estimates (Ciais et al., 2009; Gurney et al., 2005; Peylin et al., 2011; Nassar et al., 2013; Asefi-Najafabady et al., 2014). Further, the development of atmospheric transport models with increased spatial and temporal resolution makes it possible to quantify these impacts (e.g., Kawa et al., 2010; Peylin et al., 2011). Previous literature has reported the uncertainty in related inversion and forward simulation studies (Gurney et al., 2005; Peylin et al., 2011; Nassar et al., 2013). For example, Gurney et al. (2005) investigated the impact of monthly varying FFCO₂ emissions on inverted net carbon exchange and found a monthly bias of up to 50% in biospheric net fluxes in some places caused by unaccounted-for variations in fossil fuel emissions. Peylin et al. (2011) showed a seasonal uncertainty of about 2 ppm in simulated CO₂ concentration associated with uncertainty in the spatial and temporal variability in FFCO₂ emissions over Europe. Similarly, Nassar et al. (2013) reported the impact of time-varying FFCO₂ emissions on selected geographical regions during wintertime. Previous studies, however, have focused on only one or two components of the sub-annual FFCO₂ cycles, or else on limited spatial regions or time periods. Thus, a complete exploration of the space/time influence of all sub-annual variations in FFCO₂ across the globe is needed.

Inversion analysis infers the distribution of sources and sinks of CO₂ by reconciling the observed global atmospheric CO₂ concentrations at a network of sampling stations with simulated CO₂ concentrations obtained by driving an atmospheric transport model with an initial estimate of CO₂ fluxes. During this process, the interaction of temporally varying boundary CO₂ fluxes with atmospheric transport/mixing has been shown to impact the inferred surface CO₂ source/sink distribution. For example, the covariation of seasonal/diurnal biospheric fluxes and seasonal/diurnal atmospheric transport causes a significant seasonal/diurnal effect (commonly called the rectifier) on CO₂ concentrations, even if the fluxes at each grid cell average to zero across each time period (e.g., Keeling et al., 1989; Denning et al., 1995, 1996; Yi et al., 2004; Chen and Chen, 2004; Chan et al., 2008; Williams et al., 2011). The biospheric rectification is characterized by a time-mean CO₂ spatial concentration gradient, with the diurnal effect at local to regional scales caused by the interaction of diurnal biospheric fluxes with the diurnal variation in vertical mixing in the planetary boundary layer (PBL), and the seasonal rectifier effect at the global

scale resulting from the interaction of seasonal biospheric fluxes with seasonal atmospheric transport. By contrast, few studies have quantified the rectification of atmospheric CO₂ concentration associated with the sub-annual variations in FFCO₂ fluxes (diurnal, weekly and monthly).

In this paper, we test the sensitivity of simulated global atmospheric CO₂ concentration to sub-annual temporal variations in FFCO₂ emissions using a tracer transport model. The sub-annual FFCO₂ emission variability is comprised of three cyclic components: diurnal, weekly, and seasonal. The resulting surface atmospheric CO₂ concentration from these individual components and their sum are compared to simulated CO₂ concentrations driven by a “flat” (temporally invariant) FFCO₂ emissions inventory. The impact on the column-integral simulated CO₂ concentration is also examined.

The structure of this paper is as follows: Sect. 2 describes the FFCO₂ emissions and sub-annual variability, the biospheric fluxes used for comparison with the FFCO₂ emissions, the atmospheric tracer transport model employed in model simulations, and the methods for analyzing the model output. In Sect. 3, the results of the flux experiments are presented and discussed at multiple timescales. Section 4 summarizes the results and implications of this study.

2 Methods

In this study, we prescribe five global FFCO₂ emission fields that are introduced into the lowest atmospheric layer of a tracer transport model and subsequently run for four simulated years. Three years are considered a spin-up to allow FFCO₂ to reach equilibrium through the entire troposphere. The last year is used for analysis and the FFCO₂ mixing ratio is analyzed globally and at CO₂ observing sites.

2.1 FFCO₂ emissions

The FFCO₂ emissions data product, Fossil Fuel Data Assimilation System (FFDAS) version 2.0, is used as the flux boundary condition for the model simulations in this study (Asefi-Najafabady et al., 2014). The FFDAS FFCO₂ emissions were estimated using a diagnostic model (the Kaya identity, Kaya and Yokoburi, 1997), constrained by a series of spatially explicit observational data sets, which decompose emissions into population, economics, energy, and carbon intensity terms (Rayner et al., 2010). The observational data sets used in the FFDAS include a remote sensing-based nighttime lights data product, the LandScan gridded population data product, national sector-based fossil fuel CO₂ emissions from the International Energy Agency (IEA), and a recently constructed database of global power plant CO₂ emissions (Elvidge et al., 2009; Asefi-Najafabady et al., 2014).

The FFDAS emissions are produced at $0.1^\circ \times 0.1^\circ$ resolution for the years 1997 to 2010. The emissions for year 2002 are used in this study. Sub-annual temporal structure is im-

posed on these annual emissions based on two additional data sets. Diurnal and weekly cycles are derived from a global data product referred to as Temporal Improvements for Modeling Emissions by Scaling (TIMES hereafter) at $0.25^\circ \times 0.25^\circ$ resolution (Nassar et al., 2013). The monthly temporal cycle is obtained from the global data product developed by Andres et al. (2011) at a resolution of $0.1^\circ \times 0.1^\circ$ and similarly imposed on the FFDAS emissions. With these temporal structure data sets, five separate FFCO₂ emission fields are created:

1. A global $0.1^\circ \times 0.1^\circ$ FFCO₂ emission field in which only the diurnal cycle is represented (“diurnal cycle emissions” – DCE). This is accomplished by distributing the annual emission total in each grid cell evenly for every day of the year (divided by 365), and then distributing the daily total to the 3 h model simulation resolution according to the diurnal fractions from TIMES.
2. A global $0.1^\circ \times 0.1^\circ$ FFCO₂ emissions field in which only the weekly cycle is represented (“weekly cycle emissions” – WCE). This is accomplished by distributing the annual emissions in each grid cell evenly for each week of the year (divided by 52) and then distributing the weekly total according to the day-of-the-week fractions from TIMES.
3. A global $0.1^\circ \times 0.1^\circ$ FFCO₂ emission field in which only the monthly cycle is represented (“monthly cycle emissions” – MCE). This is accomplished by distributing the annual total FFCO₂ emissions in each grid cell according to the monthly fractions from Andres et al. (2011). To avoid discontinuities at the month boundaries, a cubic spline filter is applied.
4. A global $0.1^\circ \times 0.1^\circ$ FFCO₂ emission field that represents all of the sub-annual temporal structure (“all cycle emissions” – ACE). This is accomplished by applying the MCE, WCE and DCE fractions in succession with the application of the cubic spline smoother and scaling to ensure conservation of mass.
5. A global $0.1^\circ \times 0.1^\circ$ FFCO₂ emission field with no sub-annual temporal structure (“flat emissions” – FE). Hence, the annual amount in each grid cell is divided by 2920 to obtain evenly distributed emissions at 3 h model resolution.

To understand the temporal variations in the input FFCO₂ emission fields used in the simulations, we focus attention on areas of the planet with large FFCO₂ emissions, what we refer to as the “large source regions” (LSRs). These regions are located in the US (30 to 48° N, 125 to 70° W), western Europe (40 to 60° N, 10° W to 40° E) and China (20 to 45° N, 105 to 125° E).

The DCE FFCO₂ emissions over the three LSRs show a diurnal cycle (Supplement, Fig. S1) that is characterized by

smaller emissions at night and in the early morning vs. larger emissions starting at sunrise and remaining elevated until just after sunset. The DCE emissions typically reach a minimum value between midnight and 03:00 local time (LT) and a maximum value at $\sim 15:00$ LT. This pattern is expected from the diurnal variations in human activity, such as waking vs. sleeping hours and work-related activity cycles (e.g., on-road vehicle “rush” hours, starting and ending most daily work cycles). We also show the diurnal cycle of PBL height used in this study (Fig. S1), which shows similar diurnal variation to the diurnal DCE FFCO₂ emissions.

The WCE FFCO₂ emissions reflect diminished economic activity on the weekends vs. the weekdays. For most of the planet, Saturday and Sunday are the designated weekend days, but in some Middle Eastern countries, Thursday and Friday constitute the weekend days (Fig. S2).

The MCE FFCO₂ emissions reflect the different energy needs in winter vs. summer: for example, due to space heating of buildings (Fig. S3). However, the space/time patterns reflect different fossil-fuel-based energy use across the planet. For example, the FFCO₂ emissions in western Europe are larger in December and January and smaller in July and August. The US also shows peak emissions in December–January, but with a second peak in July–August. The summer peak is due to electricity-driven air-conditioning prevalent in the United States (Gregg et al., 2009). China exhibits an unusual monthly variation, with the largest FFCO₂ emissions in December followed by a sudden drop in January and February, and then an increasing trend to December. This has been attributed to uncertainty in the underlying energy consumption data, discussed in detail in Gregg et al. (2008).

To enable atmospheric transport simulation, the five FFDAS emission fields were regridded from their original $0.1^\circ \times 0.1^\circ$ spatial resolution to the $1.25^\circ \times 1^\circ$ atmospheric transport model (see Sect. 2.3) resolution (longitude \times latitude). When regridding, emissions originally emanating from land are often allocated to water-covered grid cells – an artifact typically encountered along coastlines when regridding from a fine to coarse resolution. Such a mismatch can lead to a dynamical inconsistency between the emissions and atmospheric transport. To avoid this error, we apply the “shuffling” reallocation method described in Zhang et al. (2014) for all five emissions fields. For the purposes of atmospheric transport simulations, the emissions derived from FFDAS for the year 2002 are repeated across all the years in the atmospheric transport model runs.

2.2 Biospheric fluxes

In order to place the impact of the temporal variation in FFCO₂ emissions within a larger context, an additional experiment is conducted driven by terrestrial biospheric carbon fluxes with diurnal and seasonal variations. The biospheric CO₂ flux is a recent version of that used in the TransCom experiment: CASA model net ecosystem exchange estimates

with “neutral” annual fluxes (e.g., Law, et al., 2008; Peylin et al., 2013; Randerson et al., 1997) at a $1^\circ \times 1^\circ$ spatial resolution and 3-hourly temporal resolution (referred to as “CASA fluxes” hereafter). The terrestrial biospheric fluxes have a seasonal cycle, characterized by negative values (carbon uptake from the atmosphere to land) during the growing season (late spring and summer) vs. positive fluxes (carbon release from the land to the atmosphere) during the dormant season (winter and early spring) (Fig. S3). The biospheric fluxes also contain diurnal variation with typically negative values during the daytime (dominated by photosynthetic uptake) and positive values during the night (dominated by respiration) (Fig. S1).

The biospheric fluxes are regridded from the original $1^\circ \times 1^\circ$ to the $1.25^\circ \times 1^\circ$ transport model resolution with the same shuffling method used for the FFCO₂ emission fields.

2.3 Transport model

A global tracer transport model, the Parameterized Chemical Transport Model (PCTM), is used to simulate the FFCO₂ concentrations resulting from each of the five FFCO₂ emission fields (Kawa et al., 2004, 2010). The meteorological fields from the Goddard Earth Observing System Data Assimilation System Version 5 (GEOS-5) MERRA reanalysis products are used to drive the atmospheric transport (Reineker et al., 2008). The model uses a semi-Lagrangian advection scheme (Lin and Rood, 1996); the sub-grid-scale transport includes convection and boundary layer turbulence processes (McGrath-Spangler and Molod, 2014). The model grid is run at 1.25° longitude \times 1° latitude with 72 hybrid vertical levels, and produces CO₂ concentration output every hour. The CO₂ concentration output from PCTM has been widely used in comparison with in situ and satellite measurements (Parazoo et al., 2012). It has been shown that PCTM simulates the diurnal, synoptic, and seasonal variability in CO₂ concentration well (e.g., Kawa et al., 2004, 2010; Law et al., 2008).

A total of six emission cases are run through the PCTM. The GEOS-5 meteorology has a 3 h time resolution and a constant 7.5 min time step is used in the model simulations.

2.4 Analysis methods

In this study, all five FFCO₂ simulations use the same meteorology and the same annual total FFCO₂ emissions. The only difference between the FFCO₂ simulations is the sub-annual temporal structure as described in Sect. 2.1. Hence, the resulting atmospheric FFCO₂ concentration differences are due to the differences in the time structure of the FFCO₂ emissions only. The atmospheric FFCO₂ concentration is examined in two ways: (a) near the surface (at ~ 998 hPa; in the bottom layer, which is ~ 126 m or ~ 15 hPa thick) and (b) as a pressure-weighted column integral. In order to understand how the different cyclic components of the FFCO₂ emissions

interact with the simulated atmospheric transport at multiple timescales, we present the simulated FFCO₂ concentration results for the annual mean, and individual sub-annual cycles for both near-surface and column-integral (diurnal, weekly, monthly). In addition to global difference maps, concentration differences between the cyclic and flat FFCO₂ emissions are examined at selected GLOBALVIEW-CO₂ monitoring sites (http://www.esrl.noaa.gov/gmd/ccgg/globalview/co2/co2_intro.html) (Masarie and Tans, 1995).

The impact of the FFCO₂ emissions’ sub-annual temporal structure is defined as the simulated concentration difference between each sub-annually varying FFCO₂ emission field and the FE emission field, when averaged over specific time cycles:

$$\Delta C_{it} = \frac{1}{N} \sum_{k=1}^N \left(\frac{1}{M} \sum_{j=1}^M C_{it(j,k)} - \frac{1}{M} \sum_{j=1}^M C_{if(j,k)} \right), \quad (1)$$

where ΔC_{it} is the mean concentration difference at the i th grid cell for cyclic emissions, N is the total counts of cycles over the investigated period, $C_{it(j,k)}$ is the j th hourly concentration in the k th cycle at the i th grid cell for cyclic emissions, M is the total counts of hourly periods for each cyclic emissions, and $C_{if(j,k)}$ is the j th hourly concentration in the k th cycle at the i th grid cell for flat emissions.

By utilizing Eq. (1), the impact on simulated CO₂ concentration is examined for each individual sub-annual FFCO₂ emissions cycle and their combination. Impacts include

1. the annual mean full-day concentration difference between each cyclic FFCO₂ emission and the flat emission fields, in order to explore FFCO₂ emissions rectification;
2. the annual mean afternoon (noon to 18:00 LT) concentration difference between the DCE and FE emission fields, to examine the impact at typical atmospheric monitoring times;
3. the annual daily mean concentration difference on weekdays/weekends between the WCE and FE emission fields, to examine the impact of weekly cycles;
4. the diurnal amplitude of hourly mean concentration difference over the year between the DCE and FE emission fields, to examine the impact of diurnal cycles;
5. the seasonal amplitude of monthly mean concentration difference between MCE and FE emission fields, to examine the impact of the seasonal cycles.

The amplitude of the simulated concentration differences for DCE and the MCE simulations is defined as

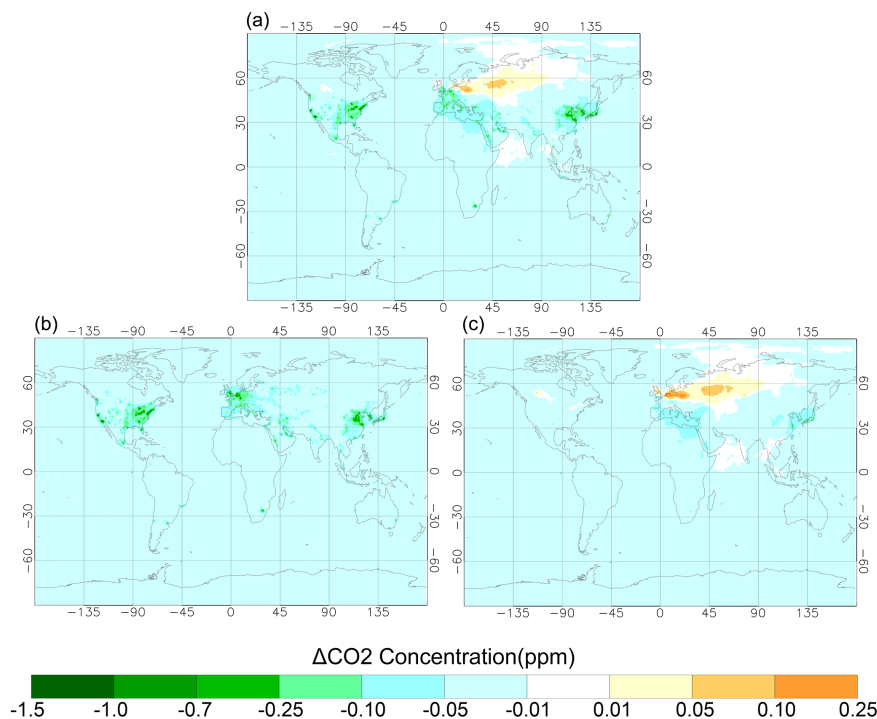


Figure 1. Simulated full-day annual mean surface FFCO₂ concentration difference between the time-varying and flat FFCO₂ emission fields. (a) ACE minus FE, (b) DCE minus FE, and (c) MCE minus FE.

$$C_{\text{amp},it} = C_{\text{max},it} \left\{ \Delta C_{itj} \Big|_{j=1,M} \right\} - C_{\text{min},it} \left\{ \Delta C_{itj} \Big|_{j=1,M} \right\}, \quad (2)$$

where $C_{\text{amp},it}$ is the amplitude at the i th grid cell, $C_{\text{max},it}$ is the maximum of the concentration differences at the i th grid cell, $C_{\text{min},it}$ is the minimum of the concentration differences at the i th grid cell, ΔC_{itj} is the mean concentration difference for the j th point of the sub-annual cycle at the i th grid cell that is defined as Eq. (1), and M is the total points of the sub-annual cycle.

3 Results and discussion

3.1 The FFCO₂ rectifier

Figure 1a shows the annual mean full-day surface FFCO₂ concentration difference between the ACE and FE emission fields (ACE minus FE). Despite the same annually integrated emissions at each grid cell, the annual mean surface concentration difference shows nonzero values, suggesting rectification of the FFCO₂ emissions. The largest negative surface FFCO₂ concentration differences (up to -1.35 ppm) are found over the LSRs, coincident with the largest fossil-fuel-based industrial activity and energy consumption. Smaller positive surface FFCO₂ concentration differences (up to 0.13 ppm) appear over north and northeastern Europe and

western Siberia. The annual mean surface FFCO₂ concentration differences between the DCE and FE and the MCE and FE are shown in Fig. 1b and c, respectively. The negative surface FFCO₂ concentration differences in Fig. 1a are primarily driven by the DCE emissions (Fig. 1b) while the positive differences are primarily driven by the MCE emissions (Fig. 1c). Figure 1a includes the contribution from the WCE emissions, but no rectification results from this emission cycle at annual scales (Fig. S4).

Over the LSRs, the diurnal FFCO₂ emissions are temporally correlated with the diurnal variation in the PBL (Fig. S1). The emissions are largest during daytime when the PBL is well mixed, so air with enriched CO₂ tends to be transported aloft. By contrast, the smaller nighttime FFCO₂ emissions are mixed into a typically shallower and stable PBL, so this lower-CO₂ air is confined closer to the surface. This covariation, when compared to the same dynamic coupling in the FE field, leads to greater FFCO₂ loss from the surface to the free troposphere in the ACE simulation, resulting in the negative annual mean surface FFCO₂ concentration difference values over the LSRs. The negative DCE rectification is up to -1.44 ppm at the grid cell scale over the western US (Fig. 1b). Note that the diurnal FFCO₂ rectifier effect shows little variation across the LSRs, due mainly to the similar diurnal amplitude of the diurnal emission fields.

The annual mean surface FFCO₂ concentration differences between the MCE and flat FE emissions are largest over the LSRs during the local winter months and small-

est during the local summer months (Fig. S3). This variation interacts with simultaneous variations in PBL variation. However, distinct from the diurnal FFCO₂ rectification, the seasonal FFCO₂ rectification shows positive values (up to 0.23 ppm) for north and northeastern Europe vs. negative values (up to -0.28 ppm) in East Asia, and a near-zero signal (no rectification) in the US (Fig. 1c). The positive rectification obtained in north and northeastern Europe to Siberia is associated with the coincidence of large wintertime FFCO₂ emissions and weak wintertime atmospheric mixing, which tends to trap CO₂-enriched air near the surface. Additionally, the greater vertical mixing in summertime interacts with the smaller summer FFCO₂ emissions, thus distributing more of the CO₂-depleted air to the free troposphere. The limited seasonal rectification in North America vs. the other LSRs is mainly due to the more complex FFCO₂ emissions seasonality, with peak emissions in both the winter and summer months as shown previously. Finally, the negative rectification in East Asia is mainly ascribed to the previously mentioned anomalous monthly FFCO₂ emissions in China (increasing trend from January to December) and their interaction with atmospheric transport. Hence, the CO₂-depleted air is confined to the surface in East Asia by the very small FFCO₂ emissions combined with the inactive atmospheric transport in January and February.

The rectification of the FFCO₂ fluxes can be compared to the well-known biosphere flux rectifier. Surface concentration differences of up to 20.35 ppm at the grid cell scale for the biospheric flux simulation (Fig. S5) are centered over the tropical land and northern mid- to high latitudes with much greater spatial extent than found for either the diurnal or seasonal FFCO₂ rectifier. Similar to the FFCO₂ rectification, the biospheric rectifier is a combination of diurnal and seasonal rectifications (e.g., Denning et al., 1995, 1996; Yi et al., 2004; Chen and Chen, 2004; Chan et al., 2008; Williams et al., 2011). For the diurnal biospheric rectification, the daytime net negative CASA fluxes typically coincide with a well-mixed PBL and greater interaction with the free troposphere. At night, this flux is typically reversed and mixed into a shallow PBL, resulting in a positive full-day annual mean surface CO₂ concentration due to the greater loss of CO₂-depleted air during the day. In the case of the seasonal biospheric rectifier, the summer net negative CASA fluxes are mixed into a thicker PBL, resulting in a strong negative surface perturbation, whereas the winter net positive CASA fluxes are mixed into a thinner PBL, resulting in a weaker positive perturbation. The two interactions combine to give a positive annual mean surface CO₂ concentration. The above analysis indicates that FFCO₂ rectification is mechanistically similar to biospheric rectification, but the FFCO₂ rectifier effect occurs mainly at local-to-regional scales, while the biosphere rectification is expressed at a larger spatial scale.

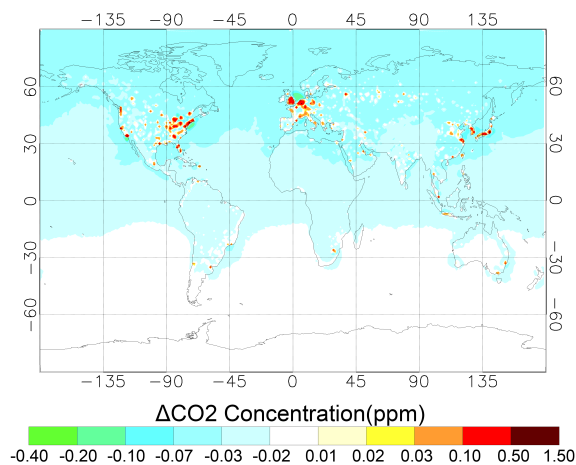


Figure 2. Simulated annual mean surface FFCO₂ concentration difference between the DCE and FE FFCO₂ emission fields (DCE minus FE), sampled during the local afternoon (12:00–18:00).

3.2 Impact on afternoon sampling

Atmospheric inversion studies of CO₂ fluxes using flask and tall tower atmospheric CO₂ measurements require consideration of CO₂ concentration sampling times (e.g., Peters et al., 2007; Dang et al., 2011). Given the importance of the simulated CO₂ concentration to the diurnal cycle of FFCO₂ emissions, we sub-sample the DCE FFCO₂ simulation output for local afternoon (noon–18:00 LT) conditions, a common sampling time for flask measurement and a chosen sampling time by inversions to avoid the difficulties associated with capturing nighttime PBL dynamics. Figure 2 presents the spatial distribution of the annual mean, afternoon-only surface FFCO₂ concentration difference between the DCE and FE fields. Values vary from -0.21 to +1.13 ppm, with larger positive values centered over the LSRs. Negative values are present over regions with low emissions, which is mainly due to the interaction of small emissions and a stable PBL at nighttime and the early morning in the DCE experiment compared to the same dynamic in the FE experiment. The afternoon and 24 h mean signals (Fig. 1b) are of opposite signs but roughly the same magnitude over the LSRs. This is due to the afternoon signal being sampled at the time of the largest afternoon emissions but also contributing the weakest surface signal to the 24 h diurnal span. The afternoon mean signal indicates that a potential bias would be incurred by ignoring the diurnal variability in the FFCO₂ emissions. It is noteworthy that the afternoon effect mainly occurs at the local scale, and has a much smaller spatial extent than the full-day diurnal rectification. This indicates that CO₂ monitoring strategies could minimize the effect of the FFCO₂ diurnal cycle when using afternoon measurements and the measurements can be taken close to large source regions for studies influenced by the diurnal cycle.

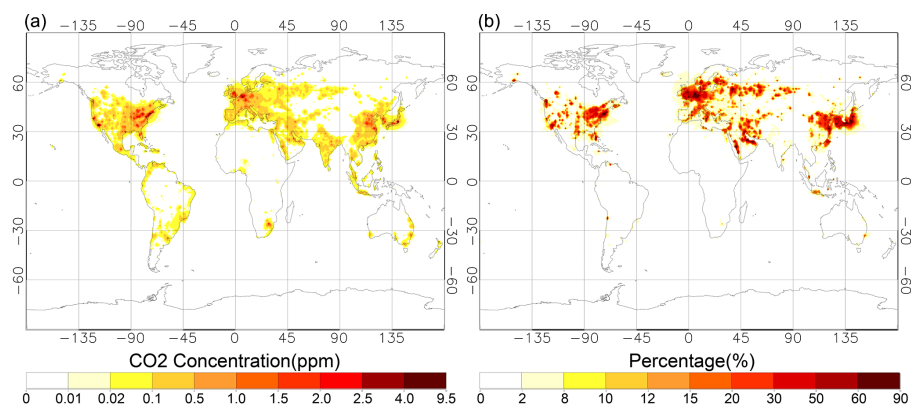


Figure 3. The diurnal amplitude of the FFCO₂ surface concentration from the DCE simulation. **(a)** The peak-to-peak diurnal amplitude of the annual mean, hourly concentration difference between the DCE and FE emission fields (DCE minus FE). **(b)** Ratio of FFCO₂ diurnal amplitude to the diurnal CO₂ amplitude of total FFCO₂ and biosphere.

3.3 Impact of the diurnal amplitude

The continuous atmospheric CO₂ measurements taken by many monitoring stations can see the complete 24 h coverage of atmospheric CO₂ concentration, and can enable the estimate of sub-daily fluxes in inversion studies using these data (e.g., Law et al., 2008). This motivates the examination of the diurnal peak-to-peak amplitude of the simulated concentration, since this parameter includes the overall daily information of the diurnal FFCO₂ concentration.

Figure 3a displays the amplitude of the annual mean diurnal surface concentration difference between the DCE and FE fields across the globe. The largest amplitude values are centered over the LSRs, with peak-to-peak values reaching 9.12 ppm in western US (−117° E, 34° N). Local sunrise is the point when the FFCO₂ concentrations reach their greatest difference. At local sunrise, the FE emissions exceed the DCE emissions, which are small prior to the increase of daytime emitting activity (Fig. S1). When combined with the minimum in vertical mixing and a shallow nighttime PBL, the resulting FFCO₂ concentration difference is negative (DCE minus FE). Local sunset, by contrast, is the point in the annual mean diurnal cycle where the differences between the DCE and FE fields are at their smallest (Fig. S1) and the DCE emissions exceed those of FE. This combines with the much greater vertical mixing and greater PBL height, and tends to ameliorate the resulting surface FFCO₂ concentration difference. Hence, the amplitude difference is driven primarily by the concentration difference at the minima of the diurnal cycle (local sunrise).

To provide context for the magnitude of the FFCO₂ diurnal amplitude, the surface FFCO₂ DCE concentration amplitude can be compared to that resulting from biosphere fluxes. This is shown in Fig. 3b, where the ratio of FFCO₂ amplitude to the total of the FFCO₂ and biosphere amplitudes is presented. Averaged over the LSRs, the diurnal amplitude of the annual mean FFCO₂ concentration accounts for more

than 15 % of the total diurnal amplitude, and this ratio rises as high as 87 % at the grid cell scale over the LSRs (corresponding to a FFCO₂ diurnal amplitude that is 5 ppm larger than the biospheric amplitude, Fig. 3b). The diurnal amplitude can be examined seasonally as well. The diurnal FFCO₂ amplitude accounts for a larger portion (up to 5 ppm) of the total diurnal variation than the diurnal biospheric amplitude in winter, when the biosphere is relatively quiescent and vertical mixing is less vigorous (Fig. S6). Overall, this result indicates that studies of diurnal atmospheric CO₂ should consider the contribution of diurnal FFCO₂ emissions, especially over LSRs and in wintertime.

3.4 Impact of the seasonal amplitude

Figure 4 shows the amplitude of monthly CO₂ concentration difference between the MCE and FE (MCE – FE) fluxes. The seasonal amplitude varies from 0.01 to 6.11 ppm, with large signals over the LSRs as seen in previous figures. Both the magnitude and spatial extent are larger than found in the diurnal case. The longer periodicity allows more time for an atmospheric signal to build up and to be advected further from the emission source regions. The seasonal maxima and minima contribute equally to the amplitude for all regions (Fig. S7). The seasonal maximum mainly occurs in December–January, driven by the larger FFCO₂ emissions during winter (Fig. S8). The seasonal minimum exhibits variable timing across the LSRs, with January for China (up to −3.42 ppm), August/September for the US (−1.09 ppm) and June/July for western Europe (−2.55 ppm). This timing is consistent with the timing of the smallest FFCO₂ emissions over each region (Fig. S8). The seasonal minimum in East Asia is, as has been mentioned, likely an artifact of the inventory statistics.

The FFCO₂ seasonal amplitude can also be compared to the seasonal biospheric amplitude, for context (Fig. 4b). The biospheric amplitudes are much larger than the FFCO₂ am-

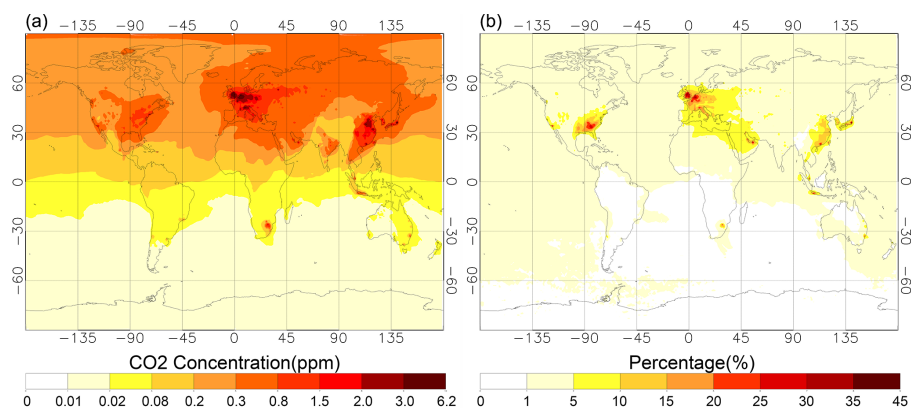


Figure 4. Seasonal amplitude of the simulated surface FFCO₂ concentration. (a) Peak-to-peak seasonal amplitude of simulated surface FFCO₂ concentration difference between the MCE and FE emission fields (MCE minus FE). (b) Ratio of FFCO₂ seasonal amplitude to the sum of the FFCO₂ and biosphere seasonal amplitude.

plitudes at the global scale, except for specific industrialized source regions in the US, western Europe and East Asia, where the FFCO₂ amplitude accounts for more than 25 % of the total seasonal amplitude. This result indicates a non-negligible local-to-regional FFCO₂ effect on seasonal amplitude of atmospheric CO₂ concentration.

3.5 Impact of the weekly cycle

The impact of the weekly cycle of FFCO₂ emissions is demonstrated here by constructing a mean weekday and mean weekend surface FFCO₂ concentration from the difference between the WCE and FE simulations (Fig. 5). As expected, the surface FFCO₂ difference values are centered over LSRs, with predominantly positive FFCO₂ concentration values for the weekdays and negative values on the weekends. The negative weekend values are a reflection of the reduced weekend FFCO₂ emissions vs. weekday activity (Nassar et al., 2013). There are a few deviations from this regular weekday/weekend pattern. First, the different definition of what constitutes weekend activity is seen over the Middle East, where the weekend is typically Thursday–Friday vs. Saturday–Sunday in most of the rest of the world. In contrast to other weekdays, Monday shows positive values only in narrow portions of East Asia. The other large source regions show negative surface FFCO₂ concentration difference values. This spatial pattern primarily reflects the residual effect of the lower weekend FFCO₂ emissions. This coherent FFCO₂ concentration difference dissipates after 24 h and is then dominated by the higher weekday FFCO₂ emissions. The residual effect of the larger Friday FFCO₂ emissions does not show up clearly in the simulated weekend FFCO₂ concentration (Fig. 5d), due to the fact that the weekend mean is constructed from 2 days and the residual effect from effect from Friday is likely negated in the 2-day mean.

3.6 Sampling at monitoring stations

Atmospheric CO₂ monitoring locations were originally situated away from fossil fuel source regions, but as FFCO₂ emissions have risen dramatically over time, they are increasingly influenced by FFCO₂ sources. A large number of monitoring stations are situated in strongly affected areas in temperate North America, western Europe and East Asia that show a strong diurnal concentration. Noteworthy are the coastal sites close to the large source regions in the US and western Europe – these show significant influence from the DCE flux component, despite the fact that these locations are assumed to represent upwind background CO₂. Time series of daily afternoon-mean CO₂ concentration differences demonstrate this influence (Fig. 6). For the sake of brevity, we focus on two stations: La Jolla, in the western US (32.9° N, 117.3° W; 10 m a.s.l.; referred to as LJO), and Lutjewad of the Netherlands (53.4° N, 6.35° E; 61 m a.s.l.; referred to as LUTDTA). The two sites were selected because they are close to LSRs (locations highlighted in the figure). A strong seasonality of up to 5 ppm for LUTDTA and up to 3 ppm for LJO is shown in the daily afternoon mean CO₂ concentration difference from the ACE simulation. Synoptic variability with approximately the same magnitude is also evident (Fig. 6b). These seasonal and synoptic effects are very similar to those presented in Peylin et al. (2011) at the station scale. Finally, a slight weekly cycle can be seen in spring and summer at both stations.

The time series can be further understood through examination of the cyclic FFCO₂ flux contributions (Fig. 6c–e). The MCE simulation shows the largest daily afternoon mean impact on CO₂ concentrations (up to 5.5 ppm) vs. smaller values for the WCE (2.2 ppm) and DCE (1.6 ppm). Large seasonality is shown in the MCE that is caused by the interaction of the monthly FFCO₂ emissions and atmospheric transport. The WCE and DCE display slight but evident seasonality that is driven mainly by the seasonal atmospheric trans-

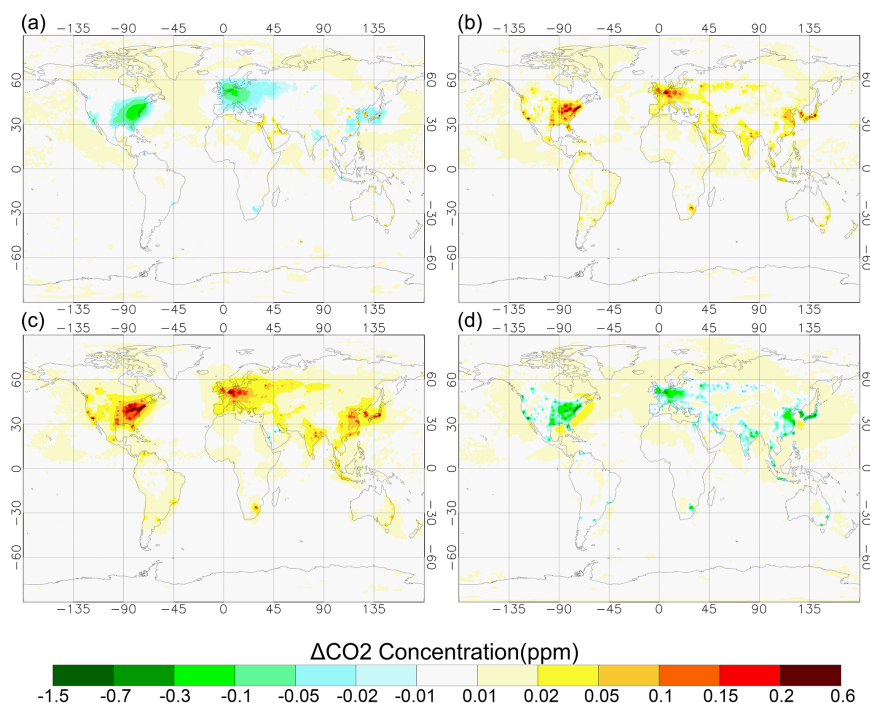


Figure 5. Simulated daily mean surface FFCO₂ concentration differences between the WCE and FE emission fields. (a) Monday, (b) Tuesday and Wednesday, (c) Thursday and Friday, and (d) Saturday and Sunday.

port. Synoptic variability is seen in the MCE (up to 4 ppm) and DCE (up to 1 ppm). The synoptic-scale effect is comparable to the results found in Peylin et al. (2011), where a ~ 5 ppm effect was found. Also, a weekly cycle is illustrated for the WCE driven by the weekly FFCO₂ emissions. These temporal patterns are common to the stations with significant response to the time cycle FFCO₂ emissions, but the magnitude is dependent on the local dynamical conditions, transport patterns and proximity of the site to the FFCO₂ sources. LJO shows a larger impact than LUTDTA in July and August, associated mainly with the large FFCO₂ emissions in summer. Differences are found in the timing of the synoptic events between the two sites, and the amplitude of the synoptic variation in the CO₂ concentration difference at LUTDTA is roughly twice that at LJO, which suggests that the synoptic events of atmospheric transport play an important role in distributing the FFCO₂ at LUTDTA.

3.7 Column-average concentration

The analysis above indicates significant CO₂ concentration response to sub-annual FFCO₂ emission variability near the surface. With the advent of satellite measurements, as well as the surface-based spectrometers of the TCCON network, it is important to examine the response of vertically averaged CO₂ concentrations to the FFCO₂ emissions. How important is sub-annual FFCO₂ emission variability to the CO₂ concentration seen from space? And what impact do these FFCO₂

emission cycles have on studies that use satellite measurements?

To answer these questions, the same analysis is performed for the simulated column-integral CO₂ concentration for all the cyclic FFCO₂ emissions as was performed for the surface. For generality, we have used simple pressure weighting to compute the column averages, rather than the vertical weighting appropriate for any particular satellite. Results indicate weak rectifier effects in the simulated column-integral FFCO₂ concentration, with ACE having negative values from -0.02 to -0.06 ppm. The ACE rectification is centered over large source regions and the MCE component represents the largest contribution overall, varying from -0.02 to -0.06 ppm (Fig. S9). The DCE exhibits similar rectification magnitudes varying from -0.02 to -0.04 ppm, but with a response covering a smaller spatial extent. The MCE rectification reflects the larger vertical and spatial effect of the monthly FFCO₂ emission variability as compared to the WCE and DCE. Compared to the surface effect, the column-integral rectification is almost an order of magnitude smaller. However, note the negative signal in western Europe from MCE, which is opposite to the positive signal at the surface (Fig. 1). Overall, the sub-annual FFCO₂ emission variability has little effect on all aspects of the column-integral CO₂ concentration.

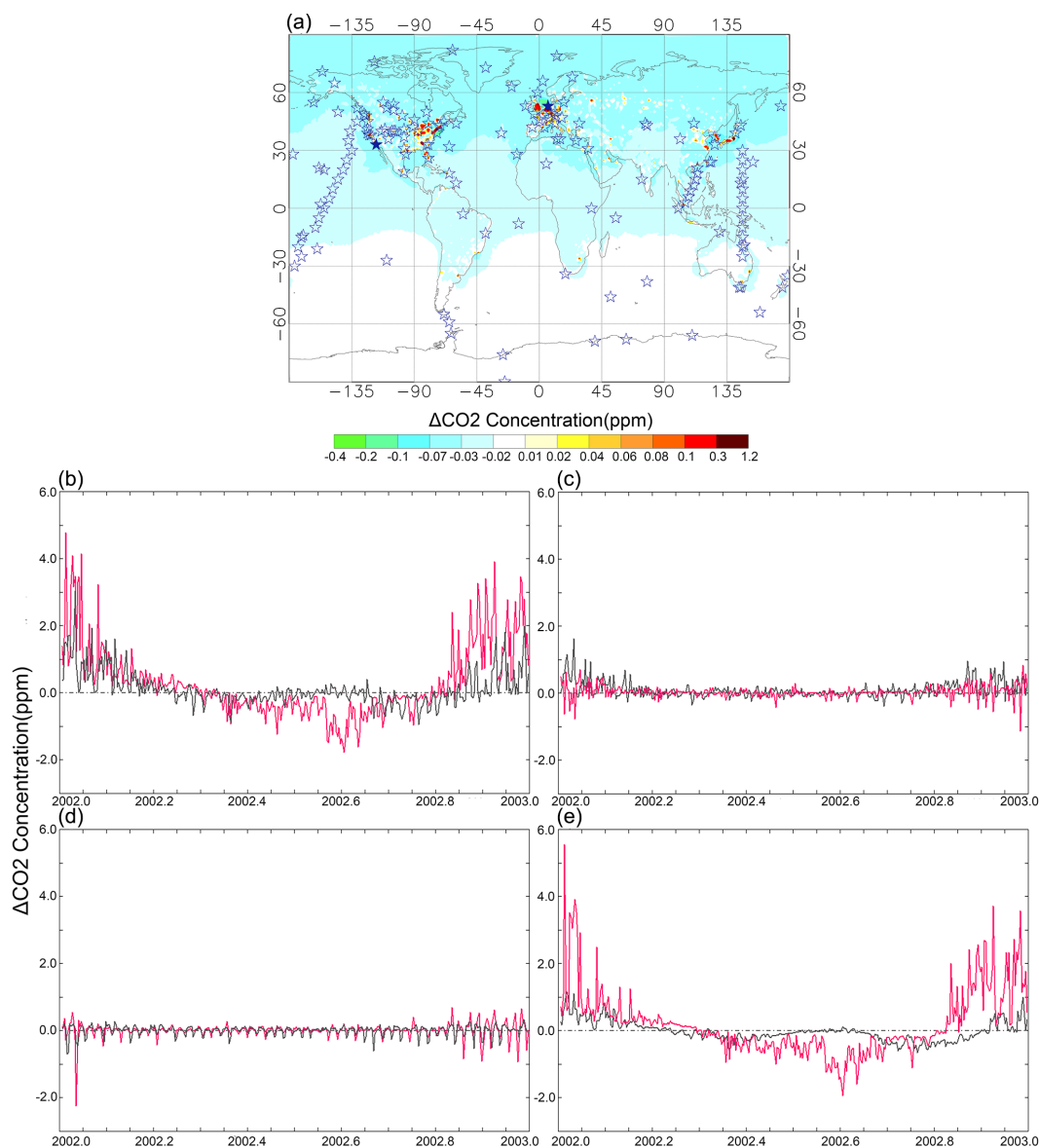


Figure 6. The simulated surface afternoon mean FFCO₂ concentration difference (12:00–18:00 LT) between the DCE and FE FFCO₂ emissions, and the locations of GlobalView monitoring stations (stars). **(a)** Daily afternoon mean FFCO₂ concentration differences between each cyclic FFCO₂ emissions field and FE emissions at two selected GlobalView stations (LJO – gray; LUTDTA – pink); **(b)** for all time cycle emissions, **(c)** for diurnal-only time cycle emission, **(d)** for weekly-only time cycle emissions and **(e)** for monthly-only time cycle emissions. Solid stars indicate the location of LJO and LUTDTA.

4 Conclusions and implication

This study investigates the impact of sub-annual FFCO₂ emissions cycles (diurnal, weekly and monthly) on the simulated CO₂ concentration. The simulated CO₂ concentrations are examined at multiple timescales over the globe as well as at GlobalView monitoring stations. When expressed as annual means, a FFCO₂ rectifier effect is found from the combination of all cycles, which varies from -1.35 to $+0.13$ ppm, centered over large source regions in the northern hemisphere. This is driven by a large negative diurnal

FFCO₂ rectification due to the interaction of large/smaller FFCO₂ emissions with vigorous/inactive PBL mixing in the daytime/nighttime, and a positive seasonal rectification in western Europe resulting from the covariance of small/larger FFCO₂ emissions in the summertime/wintertime with vigorous/inactive atmospheric transport.

The diurnal FFCO₂ emissions are also found to significantly affect the diurnal variation in simulated CO₂ concentrations at the local/regional scale, driven by the covariance of diurnally varying FFCO₂ emissions and vertical mixing. The impact on the diurnal peak-to-peak amplitude is up to

9.12 ppm, while the impact on the afternoon mean concentration is as large as +1.13 ppm at the grid cell scale. The results indicate the importance of proper temporal sampling when using/interpreting measurements affected by diurnal FFCO₂ emissions (especially those near emission regions). The small spatial extent of the afternoon effect suggests that measurements can be taken close to the large source regions when required for studies that use the afternoon-only measurements.

The monthly FFCO₂ variability results in a simulated CO₂ concentration seasonal amplitude (up to 6.11 ppm) over large source regions, caused mainly by the interaction of large/smaller FFCO₂ emissions in wintertime/summertime with inactive/vigorous PBL mixing. Significant spatial patterns are found at the regional scale, due mainly to the large difference in the seasonal variations in FFCO₂ emissions across the regions. This result suggests that attention should be given to accurate representation of seasonal profiles of regional emission inventories, particularly for large emitters like China. The diurnal response has a more limited spatial extent than the monthly response and can probably be disregarded when considering clean air oceanic sites.

The simulated CO₂ concentration at the GlobalView stations are found to be affected by all sub-annual FFCO₂ cycles, especially for sites close to large source regions. These impacts cover multiple timescales, from diurnal to seasonal, caused by the interaction/combination of the variable FFCO₂ emissions with atmospheric transport. This finding, together with the above, indicates that current inversion studies that do not incorporate sub-annually varying FFCO₂ emissions could result in biased flux estimates results due to the FFCO₂ rectifier, and that caution should be taken regarding sampling time and when choosing the locations for new sites of atmospheric CO₂ measurement.

Characterization of the column-average simulated CO₂ concentration suggests a weak impact compared to the surface signal, indicating less importance than for surface measurements. This also suggests that including the sub-annual cycles of FFCO₂ variability is not as important a concern for modeling studies using only satellite measurements.

The Supplement related to this article is available online at doi:10.5194/acp-16-1907-2016-supplement.

Acknowledgements. This work was supported by the National Science Foundation CAREER award 0846358 and NASA ROSES grant NNX11AH86G. P. Rayner is supported by an Australian professorial fellowship (DPI096309).

Edited by: M. Heimann

References

- Andres, R. J., Gregg, J. S., Losey, L., Marland, G., and Boden, T. A.: Monthly , global emissions of carbon dioxide from fossil fuel consumption, *Tellus*, 63B, 309–327, 2011.
- Asefi-Najafabady, S., Rayner, S. P. J., Gurney, K. R., McRobert, K. R. A., Song, Y., Coltin, K., Huang, J., Elvidge, C., and Baugh, K.: A multiyear, global gridded fossil fuel CO₂ emissions data product: Evaluation and analysis of results, *J. Geophys. Res.-Atmos.*, 119, 10213–10231, doi:10.1002/2013JD021296, 2014.
- Chan, D., Ishizawa, M., Higuchi, K., Maksyutov, S., and Chen J.: Seasonal CO₂ rectifier effect and large-scale extratropical atmospheric transport, *J. Geophys. Res.-Atmos.*, 113, D17309, doi:10.1029/2007JD009443, 2008.
- Chen, B. and Chen, J. M.: A vertical diffusion scheme to estimate the atmospheric rectifier effect, *J. Geophys. Res.*, 109, D04306, doi:10.1029/2003JD003925, 2004.
- Ciais, P., J., Paris, D., Marland, G., Peylin, P., Piao, S. L., Levin, I., Pregger, T., Scholz, Y., Friedrich, R., Rivier, L., Houwelling, S., Schulze, E. D., and members of the CARBOEUROPE Synthesis Team (1): The European carbon balance revisited. Part 1: fossil fuel emissions, *Glob. Change Biol.*, 16, 1395–1408, doi:10.1111/j.1365-2486.2009.02098.x, 2009.
- Dang, X., Lai, C-T., Hollinger, D. Y., Schauer, A. J., Xiao, J., Munger, J. W., Owensby, C., and Ehleringer, J. R.: Combining tower mixing ratio and community model data to estimate regional-scale net ecosystem carbon exchange by boundary layer inversion over four flux towers in the United States, *J. Geophys. Res.*, 116, G03036, doi:10.1029/2010JG001554, 2011.
- Denning, A. S., Fung, I. Y., and Randall, D. A.: Latitudinal gradient of atmospheric CO₂ due to seasonal exchange with land biota, *Nature*, 376, 240–243, 1995.
- Denning, A. S., Collatz, G. J., Zhang, C., Randall, D. A., Berry, J. A., Sellers, P. J., Colello, G. D., and Dazlich, D. A.: Simulations of terrestrial carbon metabolism and atmospheric CO₂ in a general circulation model. Part 2: simulated CO₂ concentrations, *Tellus*, 48B, 543–567, 1996.
- Elvidge, C. D., Ziskin, D., Baugh, K. E. Tuttle, B. T., Ghosh, T., Pack, D. W., Erwin, E. H., and Zhizhin, M.: A Fifteen Year Record of Global Natural Gas Flaring Derived from Satellite Data, *Energies*, 2, 595–622, 2009.
- Enting, I.: *Inverse Problems in Atmospheric Constituent Transport*, Cambridge Univ. Press, New York, USA, 2002.
- Field, C. B., Lobell, D. B., Peters, H. A., and Chiariello, N. R.: Feedbacks of terrestrial ecosystems to climate change, *Annu. Rev. Env. Resour.*, 32, 1–29, doi:10.1146/annurev.energy.32.053006.141119, 2007.
- Gregg, J. S., Andres, R. J., and Marland, G.: China: emissions pattern of the world leader in CO₂ emissions from fossil fuel consumption and cement production, *Geophys. Res. Lett.*, 35, L08806, doi:10.1029/2007GL032887, 2008.
- Gregg, J. S., Losey, L. M., Andres, R. J., Blasing, G. J., and Marland, G.: The temporal and spatial distribution of carbon dioxide emissions from fossil-fuel use in North America, *J. Appl. Meteorol. Clim.*, 48, 2528–2542, doi:10.1175/2009JAMC2115.1, 2009.
- Gurney, K. R., Law, R. M., Denning, A. S., Rayner, P. J., Baker, D., Bousquet, P., Bruhwiler, L., Chen, Y.-H., Ciais, P., Fan, S., Fung, I. Y., Gloor, M., Heimann, M., Higuchi, K., John, J., Maki, T., Maksyutov, S., Masarie, K., Peylin, P., Prather, M., Pak, B. C., Randerson, J., Sarmiento, J., Taguchi, S., Takahashi, T., and

- Yuen, C.-W.: Towards robust regional estimates of CO₂ sources and sinks using atmospheric transport models, *Nature*, 415, 626–630, 2002.
- Gurney, K. R., Chen, Y., Maki, T., Kawa, S. R., Andrews, A., and Zhu, Z.: Sensitivity of atmospheric CO₂ inversions to seasonal and interannual variations in fossil fuel emissions, *J. Geophys. Res.*, 110, D10308, doi:10.1029/2004JD005373, 2005.
- Kawa, S. R., Erickson III, D. J., Pawson, S., and Zhu, Z.: Global CO₂ transport simulations using meteorological data from the NASA data assimilation system, *J. Geophys. Res.*, 109, D18312, doi:10.1029/2004JD004554, 2004.
- Kawa, S. R., Mao, J., Abshire, J. B., Collatz, G., and Weaver, C. J.: Simulation studies for a space-based CO₂ lidar mission, *Tellus*, 62B, 759–769, 2010.
- Kaya, Y. and Yokoburi, K.: *Environment, energy, and economy: strategies for sustainability*, United Nations Univ. Press., Tokyo, Japan, ISBN 9280809113, 1997.
- Keeling, C. D., Bacastow, R. B., Carter, A. F., Piper, S. C., Whorf, T. P., Heimann, M., Mook, W. G., and Roeloffzen, H.: A three-dimensional model of atmospheric CO₂ transport based on observed winds. 1: Analysis of observed data, in *Aspects of Climate Variability in the Pacific and Western Americas*, Geophys. Monogr. Ser., vol. 55, edited by: Peterson, D. H., 165–236, AGU, Washington, D.C., USA, 1989.
- Law, R. M., Peters, W., Rödenbeck, C., Aulagnier, C., Baker, I., Bergmann, D. J., Bousquet, P., Brandt, J., Bruhwiler, L., Cameron-Smith, P. J., Christensen, J. H., Delage, F., Denning, A. S., Fan, S., Geels, C., Houweling, S., Imasu, R., Karstens, U., Kawa, S. R., Kleist, J., Krol, M. C., Lin, S.-J., Lokupitiya, R., Maki, T., Maksyutov, S., Niwa, Y., Onishi, R., Parazoo, N., Patra, P. K., Pieterse, G., Rivier, L., Satoh, M., Serrar, S., Taguchi, S., Takigawa, M., Vautard, R., Vermeulen, A. T., and Zhu, Z.: TransCom model simulations of hourly atmospheric CO₂: Experimental overview and diurnal cycle results for 2002, *Global Biogeochem. Cy.*, 22, GB3009, doi:10.1029/2007GB003050, 2008.
- Masarie, K. A. and Tans, P. P.: Extension and Integration of Atmospheric Carbon Dioxide Data into a Globally Consistent Measurement Record, *J. Geophys. Res.*, 100, 11593–11610, 1995.
- McGrath-Spangler, E. L. and Molod, A.: Comparison of GEOS-5 AGCM planetary boundary layer depths computed with various definitions, *Atmos. Chem. Phys.*, 14, 6717–6727, doi:10.5194/acp-14-6717-2014, 2014.
- Nassar, R., Napier-Linton, L., Gurney, K. R., Andres, R. J., Oda, T., Vogel, F. R., and Deng, F.: Improving the temporal and spatial distribution of CO₂ emissions from global fossil fuel emission data sets, *J. Geophys. Res.-Atmos.*, 118, 917–933, 2013.
- Oda, T. and Maksyutov, S.: A very high-resolution (1 km × 1 km) global fossil fuel CO₂ emission inventory derived using a point source database and satellite observations of nighttime lights, *Atmos. Chem. Phys.*, 11, 543–556, doi:10.5194/acp-11-543-2011, 2011.
- Parazoo, N. C., Denning, A. S., Kawa, S. R., Pawson, S., and Lokupitiya, R.: CO₂ flux estimation errors associated with moist atmospheric processes, *Atmos. Chem. Phys.*, 12, 6405–6416, doi:10.5194/acp-12-6405-2012, 2012.
- Peters, W., Jacobson, A. R., Sweeney, C., Andrews, A. E., Conway, T. J., Masarie, K., Miller, J. B., Bruhwiler, L. M. P., Pétron, G., Hirsch, A. I., Worthy, D. E. J., van der Werf, G. R., Randerson, J. T., Wennberg, P. O., Krol, M. C., and Tans, P. P.: An atmospheric perspective on North American carbon dioxide exchange: CarbonTracker, *P. Natl. Acad. Sci. USA*, 104, 18925–18930, 2007.
- Peylin, P., Houweling, S., Krol, M. C., Karstens, U., Rödenbeck, C., Geels, C., Vermeulen, A., Badawy, B., Aulagnier, C., Pregger, T., Delage, F., Pieterse, G., Ciais, P., and Heimann, M.: Importance of fossil fuel emission uncertainties over Europe for CO₂ modeling: model intercomparison, *Atmos. Chem. Phys.*, 11, 6607–6622, doi:10.5194/acp-11-6607-2011, 2011.
- Peylin, P., Law, R. M., Gurney, K. R., Chevallier, F., Jacobson, A. R., Maki, T., Niwa, Y., Patra, P. K., Peters, W., Rayner, P. J., Rödenbeck, C., van der Laan-Luijkx, I. T., and Zhang, X.: Global atmospheric carbon budget: results from an ensemble of atmospheric CO₂ inversions, *Biogeosciences*, 10, 6699–6720, doi:10.5194/bg-10-6699-2013, 2013.
- Randerson, J. T., Thompson, M. V., Conway, T. J., Fung, I. Y., and Field, C. B.: The contribution of terrestrial sources and sinks to trends in the seasonal cycle of atmospheric carbon dioxide, *Global Biogeochem. Cy.*, 11, 535–560, 1997.
- Rayner, P. J., Raupach, M. R., Paget, M., Peylin, P., and Koffi, E.: A new global gridded data set of CO₂ emissions from fossil fuel combustion: Methodology and evaluation, *J. Geophys. Res.*, 115, D19306, doi:10.1029/2009JD013439, 2010.
- Reineker, M.M., Suarez, M. J., Todling, R., Bacmeister, J., Takacs, L., Liu, H.-C., Gu, W., Sienkiewicz, M., Koster, R. D., Gelaro, R., Stajner, I., and Nielsen, J. E.: The GEOS-5 Data Assimilation System – Documentation of Versions 5.0.1, 5.1.0, and 5.2.0, NASA Technical Report Series on Global Modeling and Data Assimilation, Greenbelt, Maryland, USA, V27, 2008.
- Tans, P. P., Fung, I. Y., and Takahashi, T.: Observational constraints on the global atmospheric CO₂ budget, *Science*, 247, 1431–1438, 1990.
- Wang, R., Tao, S., Ciais, P., Shen, H. Z., Huang, Y., Chen, H., Shen, G. F., Wang, B., Li, W., Zhang, Y. Y., Lu, Y., Zhu, D., Chen, Y. C., Liu, X. P., Wang, W. T., Wang, X. L., Liu, W. X., Li, B. G., and Piao, S. L.: High-resolution mapping of combustion processes and implications for CO₂ emissions, *Atmos. Chem. Phys.*, 13, 5189–5203, doi:10.5194/acp-13-5189-2013, 2013.
- Williams, I. N., Riley, W. J., Torn, M. S., Berry, J. A., and Biraud, S. C.: Using boundary layer equilibrium to reduce uncertainties in transport models and CO₂ flux inversions, *Atmos. Chem. Phys.*, 11, 9631–9641, doi:10.5194/acp-11-9631-2011, 2011.
- Yi, C., Davis, K. J., Bakwin, P. S., Denning, A. S., Zhang, N., Desai, A., Lin, J. C., and Gerbig, C.: Observed covariance between ecosystem carbon exchange and atmospheric boundary layer dynamics at a site in northern Wisconsin, *J. Geophys. Res.*, 109, D08302, doi:10.1029/2003JD004164, 2004.
- Zhang, X., Gurney, K. R., Rayner, P., Liu, Y., and Asefi-Najafabady, S.: Sensitivity of simulated CO₂ concentration to regridding of global fossil fuel CO₂ emissions, *Geosci. Model Dev.*, 7, 2867–2874, doi:10.5194/gmd-7-2867-2014, 2014.